ISIJ International, Vol. 59 (2019), No. 9, pp. 1632–1641

Effects of Electrolysis Conditions on the Formation of Electrodeposited Invar Fe–Ni Alloys with Low Thermal Expansion

Keisuke FUKUDA,[1)] Yuki KASHIWA,[2)] Satoshi OUE,[3)] Tomio TAKASU[4)] and Hiroaki NAKANO[3)]*

1) Department of Materials Process Engineering, Kyushu University, 744, Motooka, Nishi-ku, Fukuoka-shi, 819-0395 Japan.
2) Department of Life Science, Kyushu Sangyo University, 2-3-1, Matsukadai, Higashi-ku, Fukuoka-shi, 813-8503 Japan.
3) Faculty of Engineering, Kyushu University, 744, Motooka, Nishi-ku, Fukuoka-shi, 819-0395 Japan.
4) Department of Materials Science, Kyushu Institute of Technology, 1-1, Sensui-cho, Tobata-ku, Kitakyushu-shi, 804-8550 Japan.

(*Received on January 9, 2019; accepted on February 27, 2019; originally published in Tetsu-to-Hagané, Vol. 105, 2019, No. 1, pp. 55–63*)

To elucidate the effects of the electrolysis conditions on the formation of electrodeposited invar Fe–Ni alloys with low thermal expansion, Fe–Ni electrodeposition was performed at 10–5 000 $A \cdot m^{-2}$ and 5×10^5 $C \cdot m^{-2}$ in an agitated solution containing $NiSO_4$, $NiCl_2$, $FeSO_4$, H_3BO_3, $C_7H_4NNaO_3S$, and $C_3H_4O_4$ at 40°C–60°C. In the low-current-density region, the Ni content in the deposits significantly decreased with increasing current density, reached a minimum, and then increased after reaching the diffusion-limiting current density for Fe deposition. With the increasing concentration of $FeSO_4$ in the solution, the Ni content in the deposits decreased in the lower-current-density region, reached a constant at a moderate current density, and then began to increase at higher current density. As a result, the current density range in which the Ni content in the deposits reached a minimum and remained constant became wider with increasing $FeSO_4$ concentration. With the decreasing pH of the solution, since the partial polarization curve for H_2 evolution and the total polarization curve shifted to a higher-current-density region, the curve of the Ni content in the deposits as a function of the current density shifted toward a higher current density. The change in the composition of the Fe–Ni alloy deposits because of the electrolysis conditions can be explained by the changes in the total polarization curve and the partial polarization curves for Fe and Ni deposition and H_2 evolution.

KEY WORDS: invar alloy; iron-nickel alloys; electrodeposition; anomalous codeposition; polarization curve; partial polarization curve; current efficiency; composition of deposits.

1. Introduction

The thermal expansion coefficients of Fe–Ni alloys change according to the alloy composition, reaching a minimum at a Ni content of 36 mass%. The Fe–36mass%Ni alloy is called the invar alloy,[1,2)] and owing to its low thermal expansion, it has been widely used in electronic communication devices such as semiconductor lead frames and package components of optical fibers.[3)] The invar alloy is now produced by manufacturing processes such as melting and casting methods, rolling, and mechanical working, but these conventional manufacturing processes provide limited shapes and dimensional accuracy in the final products. Therefore, when this invar alloy can be produced by electrodeposition, products can be deposited in a wider variety of shapes, and the manufacturing cost decreases.[4)] The fine processing method combined with electrodeposition and photolithography enables manufacturing of fine products with a high aspect ratio and high dimensional accuracy, which is impossible with traditional methods.

On the other hand, the electrodeposition of the Fe–Ni alloy shows a specific behavior of anomalous codeposition, in which electrochemically less-noble Fe deposits preferentially over nobler Ni.[5–18)] To explain the mechanism underlying the anomalous codeposition of the Fe–Ni alloy, two different models have been proposed. In the suppression model,[5)] the deposition of nobler Ni is suppressed owing to the preferential formation and adsorption of the hydroxide of less-noble Fe. The anomalous deposition model depends on the difference between the dissociation constants of $FeOH^+$ and $NiOH^+$.[6)] Since the thermal expansion coefficient of the Fe–Ni alloy significantly depends on the composition, controlling the alloy composition to have a Ni content of 36 mass% is essential.[19–22)] Therefore, it is important to clarify the effects of the electrolysis conditions on the composition of the deposited Fe–Ni alloy. In this study, the fundamental parameters of electrodeposition, such as the solution composition, pH, temperature, and stirring, were changed, and the effects of these conditions on the composition of the deposits were investigated. The changes in the composition and current efficiency of the deposited alloy owing to the electrolysis conditions were explained via the changes in the total polarization curve and the partial polarization curves

* Corresponding author: E-mail: nakano@zaiko.kyushu-u.ac.jp
DOI: https://doi.org/10.2355/isijinternational.ISIJINT-2019-023

for Fe and Ni deposition and hydrogen evolution during Fe–Ni alloy deposition.

2. Experimental

Table 1 shows the electrolyte composition and electrolysis conditions for the Fe–Ni alloy deposition. The electrolytic solution was prepared by dissolving reagent-grade $NiSO_4 \cdot 6H_2O$ (0.95 mol·dm^{-3}), $NiCl_2 \cdot 6H_2O$ (0.17 mol·dm^{-3}), $FeSO_4 \cdot 7H_2O$ (0.296–0.507 mol·dm^{-3}, standard condition: 0.394 mol·dm^{-3}), H_3BO_3 (0.49 mol·dm^{-3}), $C_7H_4NNaO_3S$ (saccharin sodium, 0.008 mol·dm^{-3}), and $C_3H_4O_4$ (malonic acid, 0.05 mol·dm^{-3}). The pH was adjusted to 1.5, 2.4, and 3.0 (standard condition: 2.4) using sulfuric acid and sodium hydroxide.

Electrodeposition was conducted in solutions agitated at 250 rpm using a magnetic stick-shaped stirrer with a length of 39 mm under coulostatic (10^5 C·m^{-2}) and galvanostatic (10–5 000 A·m^{-2}) conditions at 40°C–60°C. In some experiments, electrodeposition was performed in unagitated solutions to investigate the effect of stirring. Brass and platinum sheets measuring 2 cm × 1 cm were used as the cathode and anode, respectively. Since Fe^{2+} ions are oxidized to Fe^{3+} ions at the anode during deposition, an H-section cell in which the catholyte was separated from the anolyte using a glass filter was used in conducting the electrolysis. The amounts of catholyte and anolyte were 0.45 and 0.05 dm^{-3}, respectively. The deposits were dissolved from the cathode using nitric acid. Both Fe and Ni were quantitatively analyzed by inductively coupled plasma spectroscopy, and the Ni content in the deposits and the cathode current efficiency for Fe–Ni alloy deposition were calculated. The current efficiency for hydrogen evolution was determined by subtracting the current efficiency for Fe and Ni deposition from 100%. The partial current densities for Fe and Ni deposition and hydrogen evolution were calculated by multiplying the total current density by each current efficiency. The cathode potentials during deposition were measured against a saturated Ag/AgCl reference electrode (0.199 V vs. NHE, 25°C). In the polarization curves presented herein, the potentials are plotted with reference to the NHE.

Table 1. Solution compositions and electrolysis conditions.

$NiSO_4 \cdot 6H_2O$ (mol·dm^{-3})	0.95
$NiCl_2 \cdot 6H_2O$ (mol·dm^{-3})	0.17
H_3BO_3 (mol·dm^{-3})	0.49
$FeSO_4 \cdot 7H_2O$ (mol·dm^{-3})	0.296–0.507
Saccharin sodium (mol·dm^{-3})	0.008
Malonic acid (mol·dm^{-3})	0.05
Current density (A·m^{-2})	10–5 000
Temperature (°C)	40, 50, 60
Amount of charge (C·m^{-2})	10^5
pH	1.5, 2.4, 3.0
Cathode	Brass (1×2 cm^2)
Anode	Pt (1×2 cm^2)
Stirrer	250 rpm

3. Results and Discussion

3.1. Effect of the $FeSO_4$ Concentration on the Composition and Current Efficiency of the Deposited Alloy

Figure 1 shows the Ni content in the Fe–Ni alloys deposited at various current densities from the solutions containing $FeSO_4$ at different concentrations. The broken line in the figure shows the composition reference line (CRL) of Ni, which means that the Ni content in the solution is identical to that in the deposits. If the Ni content in the deposits is greater than the CRL, normal codeposition occurs, wherein the electrochemically nobler Ni is preferentially deposited over Fe. By contrast, if the Ni content in the deposits is less than the CRL, anomalous codeposition occurs, wherein the less-noble Fe is preferentially deposited over Ni. In all solutions containing $FeSO_4$ at different concentrations, the Ni content in the deposits was greater than the CRL in the low-current-density region of approximately 10 A·m^{-2}, indicating normal codeposition. Meanwhile, the Ni content in the deposits greatly decreases with increasing current density, resulting in a shift toward the anomalous codeposition region. The Ni content in the deposits reaches a minimum value at current densities of 200 to 500 A·m^{-2} and then increases as the current density further increases. Focusing on the difference in the $FeSO_4$ concentration, as this concentration increases, the curve showing the relationship between the Ni content in the deposits and the current density shifts toward a lower current density in the low-current-density region of 10 to 100 A·m^{-2}, whereas it shifts toward a higher current density in the high-current-density region above 1 000 A·m^{-2}. In the current density region of 200 to 500 A·m^{-2}, the change in the Ni content in the deposits as a function of current density becomes small with increasing $FeSO_4$ concentration.

Figure 2 shows the current efficiency for Fe–Ni alloy deposition at various current densities from the solutions containing $FeSO_4$ at different concentrations. In all of these solutions, the current efficiency for Fe–Ni alloy deposition increases with the current density, reaches a constant value at 2 000 A·m^{-2}. The current efficiency is higher in the higher concentration solution than that in the lower-con-

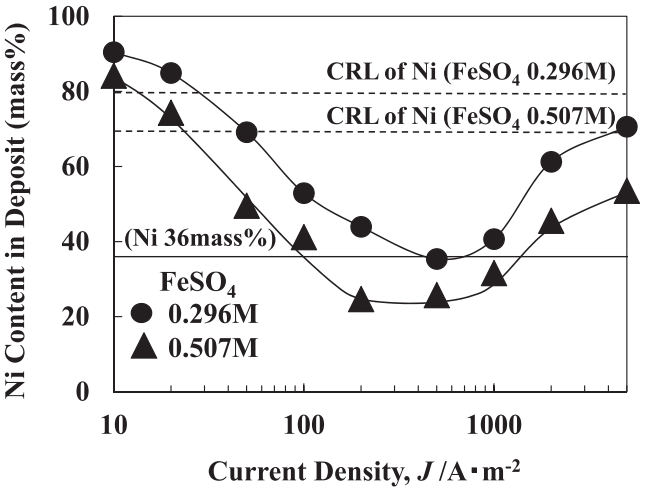

Fig. 1. Ni content in Fe–Ni alloys deposited at various current densities from solutions containing $FeSO_4$ at different concentrations [pH 2.4, 50°C, 250 rpm, 10–5 000 A·m^{-2}].

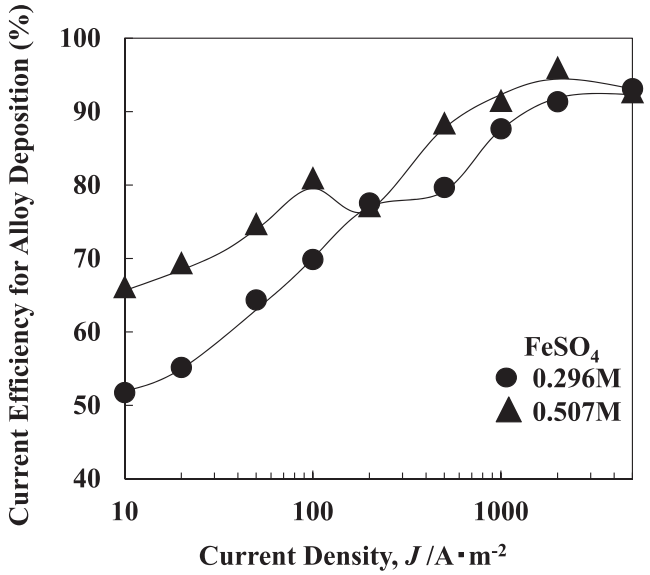

Fig. 2. Current efficiency for Fe–Ni alloy deposition at various current densities from solutions containing $FeSO_4$ at different concentrations [pH 2.4, 50°C, 250 rpm, 10–5 000 $A \cdot m^{-2}$].

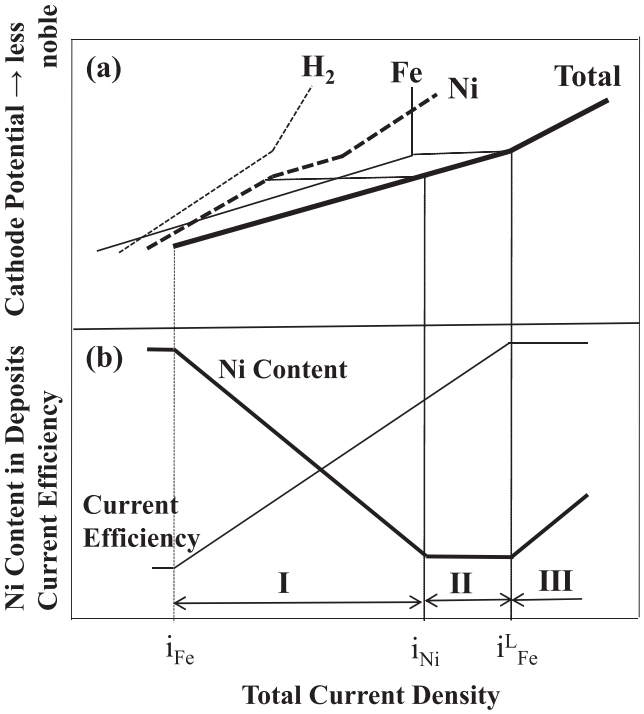

Fig. 3. Schematic diagram of the correspondence between the current density–alloy composition and current density–current efficiency curves (b) and the polarization curves for Fe–Ni alloy deposition (a).

centration solution in the current density region of less than 1 000 $A \cdot m^{-2}$. In a solution containing 0.507 $mol \cdot dm^{-3}$ of $FeSO_4$, the current efficiency decreases once at 200 $A \cdot m^{-2}$, where the Ni content in the deposits reaches a minimum, as shown in Fig. 1.

The total polarization curve and the partial polarization curves for Fe and Ni deposition and hydrogen evolution in Fe–Ni alloy deposition were estimated from the current density dependence of the composition and current efficiency of the Fe–Ni alloy deposition, as shown in Figs. 1 and 2. **Figure 3** shows a schematic diagram of the correspondence between the current density–alloy composition and the current density–current efficiency curves (b) and the polarization curves for Fe–Ni alloy deposition (a). There are three regions from the viewpoint of the change in the Ni content in the deposits. At total current densities below the total current density at which Fe begins to deposit (i_{Fe}), the Ni content in the deposits is high because the electrochemically nobler Ni is preferentially deposited over Fe. However, at total current densities above i_{Fe}, the partial current density for Fe deposition increases, and Ni deposition is suppressed by Fe deposition, causing the slope of the partial polarization curve for Ni deposition to be gentler than that of Fe deposition. Therefore, in region I, where the total current density is higher than i_{Fe}, Ni deposition is significantly suppressed with the increasing total current density, resulting in a decrease in the Ni content of the deposits. At total current densities above i_{Fe}, when the slope of the partial polarization curve for hydrogen evolution is gentler than those of Fe and Ni deposition, the current efficiency for alloy deposition increases with the current density. In region II, where the slope of the partial polarization curve for Ni deposition becomes identical to that of Fe deposition at total current densities above the total current density at which Ni deposition begins to increase rapidly (i_{Ni}), the Ni content in the deposits is almost constant. In region III, where the total current density is higher than the total current density at which Fe deposition approaches the diffusion limitation (i^L_{Fe}), Fe deposition reaches the diffusion limitation of Fe^{2+} ions, but Ni deposition does not reach the diffusion-limited current density of Ni^{2+} ions. As a result, the Ni content in the deposits increases with the current density. If the current density increases further and Ni deposition also reaches the diffusion limitation of Ni^{2+} ions, the Ni content in the deposits should increase to the CRL and become constant. However, in this study, the Ni content in the deposits increases with the current density in the high-current-density region but does not reach the CRL, as shown in Fig. 1, indicating that Ni deposition has not yet reached the diffusion-limited current density of Ni^{2+} ions. On the other hand, hydrogen evolution seems to reach the diffusion limitation of H^+ ions, but hydrogen evolves via the electrolysis of H_2O at a less noble potential. As a result, the current efficiency for alloy deposition becomes to be constant with the increasing current density at current densities above i^L_{Fe}.

Figure 4 shows the total polarization curve and partial polarization curves for Fe and Ni depositions and hydrogen evolution for the Fe–Ni alloy deposition in the solution containing 0.507 $mol \cdot dm^{-3}$ of $FeSO_4$. At potentials of −0.45 to −0.7 V, the increase in the partial current density for Ni deposition is gentler than that for Fe deposition. However, the partial current density for Ni deposition increases rapidly at approximately −0.7 to −0.77 V. Although Fe deposition approaches the diffusion limitation of Fe^{2+} ions at approximately −0.77 V, Ni deposition continues to increase at −0.77 to −1.23 V, indicating that Ni deposition does not yet reach the diffusion limitation of Ni^{2+} ions. Although the Ni content in the deposits increases with the current density in the high-current-density region, as shown in Fig. 1, it does not actually reach the CRL, indicating that the diffusion limitation of Ni^{2+} ions is attained in the total-current-density

region above 5 000 $A \cdot m^{-2}$. As mentioned above, Fe deposition reaches the diffusion-limited current density of Fe^{2+} ions at a less noble potential than Ni deposition. The slope of the partial polarization curve for hydrogen evolution is gentler than those of Fe and Ni depositions. The feature of the polarization curve mentioned above is identical to the schematic diagram of the total polarization curve and the partial polarization curves for Fe and Ni depositions and hydrogen evolution in Fe–Ni alloy deposition shown in Fig. 3(a).

It is well known that iron-group metals such as Fe, Co, and Ni inherently do not begin to deposit at their equilibrium potential and require an overpotential for deposition.[23–28] The minimum overpotential required to initiate the deposition of iron-group metal results from the rate-determining step of the multi-step reduction of iron-group metal ions. The series of reactions below have been proposed as the deposition process for iron-group metals.[15,16] M and the subscript ad in the reaction formula denote the iron-group metal and adsorption state, respectively.

$$M^{2+} + OH^- = MOH^+ \quad \cdots\cdots (1)$$

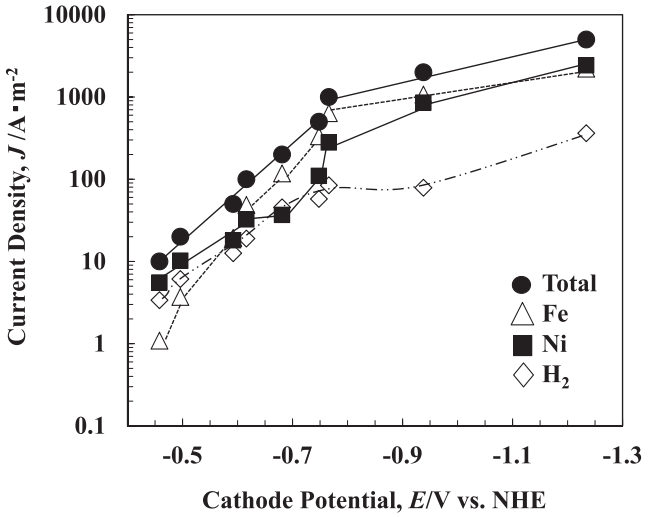

Fig. 4. Total and partial polarization curves for Fe–Ni alloy deposition [0.507 M $FeSO_4$, pH 2.4, 50°C, 250 rpm, 10–5 000 $A \cdot m^{-2}$].

$$MOH^+ + e^- \rightarrow MOH_{ad} \quad \cdots\cdots (2)$$

$$MOH_{ad} + e^- = M + OH^-. \quad \cdots\cdots (3)$$

The deposition of the iron-group metals proceeds through the adsorption intermediate of MOH_{ad}, as shown in Eqs. (2)–(3) above. In addition, the reaction in Eq. (2) becomes the rate-determining step, which shows that the adsorption sites for the MOH_{ad} intermediate are limited on the cathode. The dissociation constants of $FeOH^+$ and $NiOH^+$ are 5.78×10^{-8} and 4.50×10^{-5},[6] respectively, indicating that the concentration of $FeOH^+$ in the cathode layer is 1 000 times higher than that of $NiOH^+$ during deposition. Therefore, during the Fe–Ni alloy deposition, the adsorption sites for $NiOH_{ad}$ are deprived by $FeOH_{ad}$. As a result, the reduction of $NiOH^+$ described by Eq. (2) during Fe–Ni alloy deposition is more significantly suppressed than that from a single-component Ni solution. Therefore, Ni deposition is suppressed only in the case of codeposition with Fe, resulting in anomalous codeposition. The increase in the partial current density for Ni deposition is gentler than that for Fe deposition, as shown in Fig. 4, because the reduction of $NiOH^+$ is suppressed by $FeOH_{ad}$. On the other hand, the deposition rate of Ni increases rapidly at approximately −0.7 to −0.77 V (Fig. 4). This rapid increase is attributed to the release of the adsorption sites for $NiOH_{ad}$ that had been deprived by $FeOH_{ad}$. This release is due to the decrease in the coverage of $FeOH_{ad}$ because the reduction of Fe^{2+} ions approaches the diffusion limitation of Fe^{2+}, and the rate of reduction from $FeOH_{ad}$ to Fe increases. The current efficiency for Fe–Ni alloy deposition decreases once at 200 $A \cdot m^{-2}$ (Fig. 2) because the suppressive effect of $FeOH_{ad}$ on Ni deposition becomes large.

Figure 5 shows the partial polarization curves for Fe deposition (a), Ni deposition (b), and H_2 evolution (c) from the Fe–Ni alloy solutions containing $FeSO_4$ at different concentrations. The partial polarization curve for Fe deposition is rarely affected by the $FeSO_4$ concentration at partial current densities less than 100 $A \cdot m^{-2}$, and the potential at which Fe deposition approaches the diffusion limitation of Fe^{2+} ions shifts from −0.7 to −0.8 V with the increasing $FeSO_4$ concentration. In other words, it is difficult for Fe

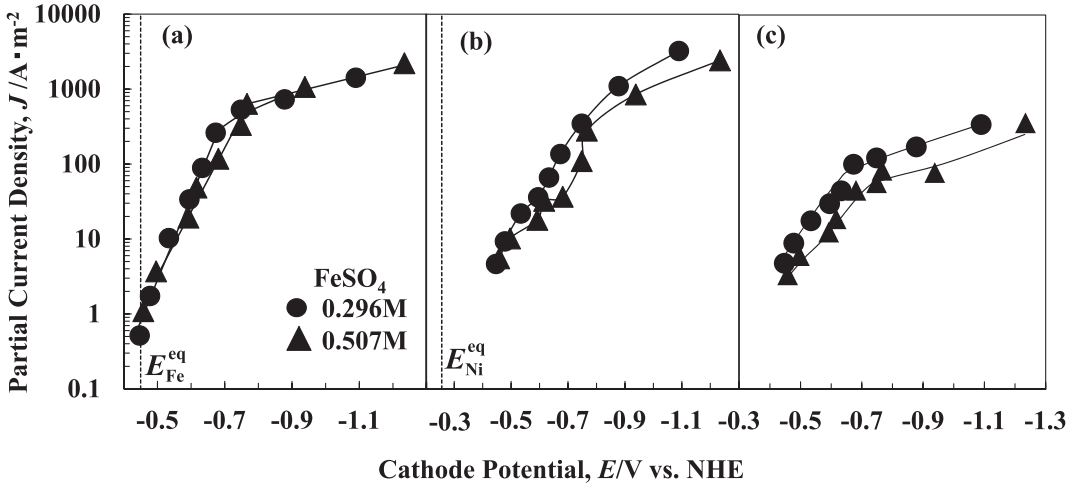

Fig. 5. Partial polarization curves for Fe (a) and Ni (b) depositions and H_2 evolution (c) from the Fe–Ni alloy solutions containing $FeSO_4$ at different concentrations [pH 2.4, 50°C, 250 rpm, 10–5 000 $A \cdot m^{-2}$].

deposition to reach the diffusion limitation of Fe^{2+} ions with the increasing $FeSO_4$ concentration [Fig. 5(a)]. On the other hand, the potential for Ni deposition was polarized with the increasing $FeSO_4$ concentration at low partial current densities of 10 to 100 $A \cdot m^{-2}$ [Fig. 5(b)]. That is, Ni deposition was increasingly suppressed with the increasing $FeSO_4$ concentration in the low-current-density region. The deposition rate of Ni rapidly increases at -0.77 to -0.88 V and at -0.7 to -0.77 V in the solutions containing 0.296 and 0.507 $mol \cdot dm^{-3}$ of $FeSO_4$, respectively. The potential for hydrogen evolution was increasingly polarized with the increasing $FeSO_4$ concentration, similar to that for Ni deposition, showing that the hydrogen evolution was more suppressed. Typically, hydrogen does not begin to evolve at the equilibrium potential, similar to the iron-group metals mentioned above, which is attributed to the slow elementary process present in hydrogen evolution.[23,29] The elementary process, which is the rate-determining step for hydrogen evolution, is the reduction through the adsorption intermediate H_{ad}, and the slow elementary process means that the adsorption sites for H_{ad} (*i.e.*, the active sites for hydrogen evolution) are limited. Therefore, the potential for hydrogen evolution is polarized by foreign substances (*i.e.*, the suppressive agents for hydrogen evolution), which preferentially adsorb onto the adsorption sites for H_{ad}, thereby decreasing the number of available sites. In this study, $FeOH_{ad}$ seems to suppress hydrogen evolution, and this suppressive effect increases with the $FeSO_4$ concentration. The current efficiency for Fe–Ni alloy deposition is higher in a solution containing a higher concentration of $FeSO_4$ in the current density region below 1 000 $A \cdot m^{-2}$, as shown in Fig. 2, because the suppressive effect on the hydrogen evolution increases with the $FeSO_4$ concentration.

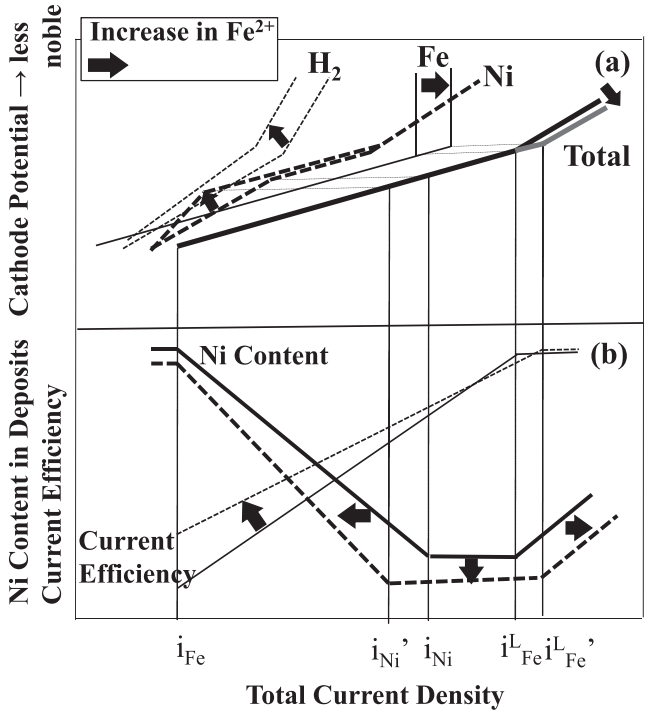

Fig. 6. Schematic diagram of the changes in the polarization curves for Fe–Ni alloy deposition (a) and current density–alloy composition and current density–current efficiency curves (b) with increasing Fe^{2+} ion concentration.

The effects of $FeSO_4$ concentration on the current density dependence of the composition and current efficiency of Fe–Ni alloy deposition were investigated from the shape of the total polarization curve and the three partial polarization curves. **Figure 6** shows a schematic diagram of the changes in the polarization curves for the Fe–Ni alloy deposition (a) and current density–alloy composition and current density–current efficiency curves (b) with the increasing Fe^{2+} ion concentration. In the low-current-density region of i_{Fe} to i_{Ni}, since Ni deposition is increasingly suppressed with the increasing $FeSO_4$ concentration, the curve of the Ni content in the deposits as a function of current density shifts toward a lower current density. On the other hand, with the increasing $FeSO_4$ concentration, the total current density i^L_{Fe} at which Fe deposition approaches the diffusion limitation of Fe^{2+} ions increases to i^L_{Fe}'. As a result, this curve in the high-current-density region above i^L_{Fe} shifts toward a higher current density. That is, the current density at which the Ni content in the deposits begins to increase with the current density increases. As mentioned above, region II, in which the Ni content in the deposits becomes almost constant, broadens with the increasing $FeSO_4$ concentration. If the electrolysis conditions are fixed to obtain the Fe–36mass%Ni alloy in region II, the invar alloy can be produced in a wider current density region. On the other hand, with the increasing $FeSO_4$ concentration, the partial polarization curve for hydrogen evolution is polarized, thus increasing the current efficiency for Fe–Ni alloy deposition.

3.2. Effect of pH on the Composition and Current Efficiency of the Deposited Alloy

Figure 7 shows the Ni content in Fe–Ni alloys deposited at various current densities from solutions of different pH values. In this experiment, the current density was fixed at 100 to 1 000 $A \cdot m^{-2}$ to focus on region II, in which the Ni content in the deposits becomes almost constant. In all solutions, the Ni content in the deposits decreases with increasing current density in the low-current-density region.

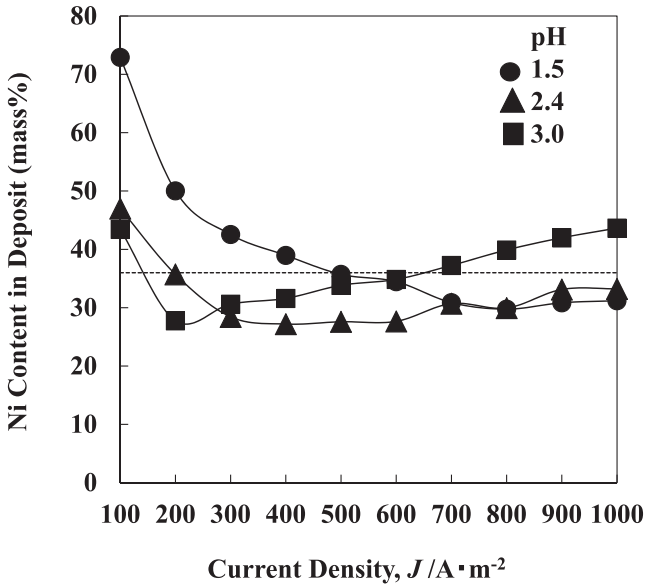

Fig. 7. Ni content in Fe–Ni alloys deposited at various current densities from solutions of different pH values [0.394 M $FeSO_4$, 50°C, 250 rpm, 100–1 000 $A \cdot m^{-2}$].

Specifically, at low current densities of 100 to 200 A·m^{-2}, the Ni content in the deposits decreases with increasing pH. In a solution of pH 3.0, the Ni content in the deposits reaches a minimum at 200 A·m^{-2} and increases as the current density further increases, whereas in a solution of pH 1.5, the Ni content in the deposits is constant at 700 to 1 000 A·m^{-2}, showing no increase in the Ni content. In a solution of pH 2.4, the Ni content in the deposits is almost constant at 300 to 600 A·m^{-2} and somewhat increases as the current density further increases. That is, regions I, II, and III, depicted in Fig. 3, are present for solutions of pH 2.4 and 3.0, and only regions I and II are observed for a solution of pH 1.5. At a high-current-density of 1 000 A·m^{-2}, the Ni content in the deposits increases with increasing pH, showing the opposite trend to that of low current densities of 100 to 200 A·m^{-2}.

Figure 8 shows the current efficiency for the Fe–Ni alloy deposited at various current densities from solutions of different pH values. The current efficiency for the alloy deposition increases with the current density in all of the various pH solutions. In addition, the current efficiency increases with pH at all current densities.

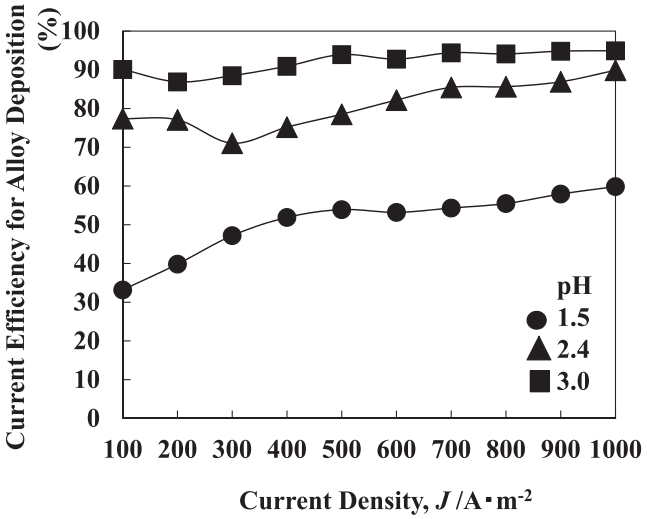

Fig. 8. Current efficiency for Fe–Ni alloy deposition at various current densities from solutions of different pH values [0.394 M $FeSO_4$, 50°C, 250 rpm, 100–1 000 A·m^{-2}].

Figure 9 shows the partial polarization curves for Fe deposition (a), Ni deposition (b), and H_2 evolution (c) from the Fe–Ni alloy solutions of different pH values. The partial polarization curves for Fe and Ni deposition shift slightly in the noble potential direction with the decreasing pH to 1.5. However, the partial polarization curves at pH 2.4 and 3.0 are hardly different. By contrast, the partial polarization for hydrogen evolution significantly changes depending on pH. Specifically, the partial polarization for hydrogen evolution shifts toward a higher current density with the decreasing pH.

The effect of the solution pH on the current density dependence of the composition and current efficiency of Fe–Ni alloy deposition was also examined from the shape of the total polarization curve and partial polarization curves. **Figure 10** shows a schematic diagram of the changes in the polarization curves for Fe–Ni alloy deposition (a) and current density–alloy composition and current density–current efficiency curves (b) with decreasing pH. The partial polarization curves of Fe and Ni in Fe–Ni alloy deposition change slightly depending on the pH, but the degree of change is significantly smaller than that of the partial polarization curves for hydrogen evolution (Fig. 9). Therefore, in the schematic diagram of the polarization curve for Fe–Ni alloy deposition shown in Fig. 10(a), only the partial polarization curve for hydrogen evolution and the total polarization curve are expected to change in the direction indicated by the arrow in this figure with decreasing pH. Since the total current density i_{Fe} at which Fe begins to deposit increases to i_{Fe}' with decreasing pH, the current density at which the Ni content in the deposits begins to decrease shifts toward a higher current density. Since the total current density i^{L}_{Fe} at which Fe deposition reaches the diffusion limitation of Fe^{2+} ions increases to i^{L}_{Fe}' with decreasing pH, the current density at which the Ni content in the deposits begins to increase shifts toward a higher current density. In other words, the curve of the Ni content in the deposits as a function of current density shifts toward a higher current density with decreasing pH. Therefore, with

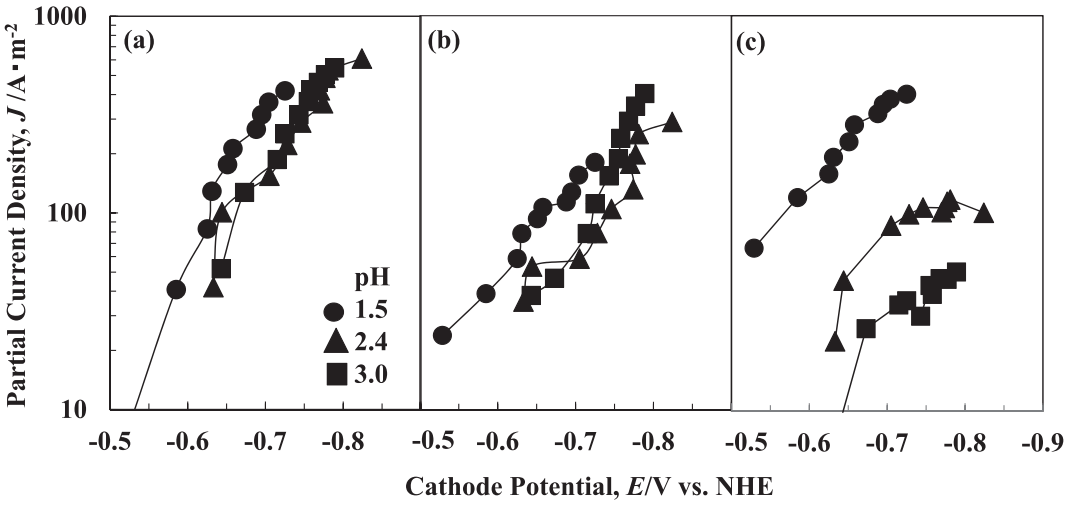

Fig. 9. Partial polarization curves for Fe (a) and Ni (b) depositions and H_2 evolution (c) from solutions of different pH values [0.394 M $FeSO_4$, 50°C, 250 rpm, 100–1 000 A·m^{-2}].

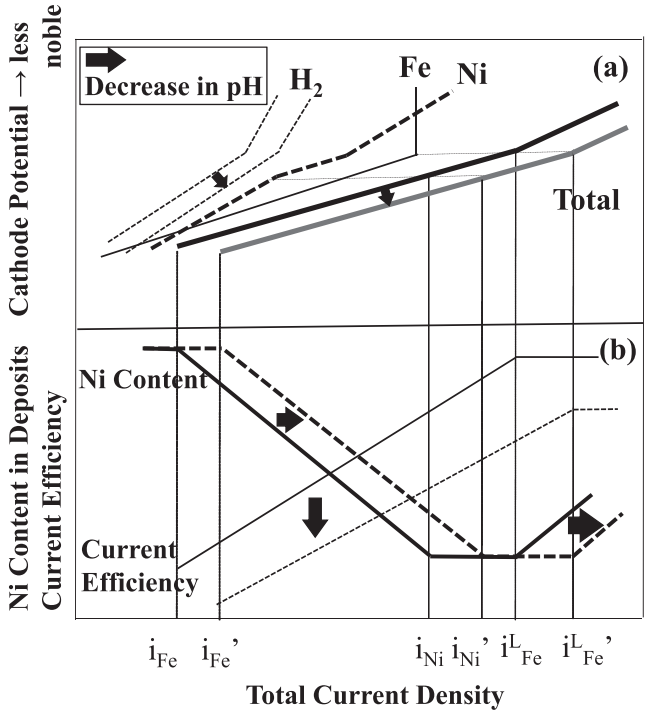

Fig. 10. Schematic diagram of the changes in the polarization curves for Fe–Ni alloy deposition (a), current density–alloy composition and current density–current efficiency curves (b) with decreasing pH.

decreasing pH, the Ni content in the deposits increases at a low current density of 100 to 200 A·m^{-2}, and it decreases at a high-current-density of 1 000 A·m^{-2} (Fig. 7). On the other hand, with decreasing pH, the current efficiency for Fe–Ni alloy deposition decreases over the entire current density region because the partial polarization curve for hydrogen evolution shifts toward a higher current density.

3.3. Effect of Temperature on the Composition and Current Efficiency of the Deposited Alloy

Figure 11 shows the Ni content in Fe–Ni alloys deposited at various current densities from the solutions at different temperatures. In the solutions at all temperatures, the Ni content in the deposits decreases with increasing current density in the low-current-density region. The Ni content in the deposits increases with temperature at a current density of 100 to 400 A·m^{-2}. In the solutions at all temperatures, the Ni content in the deposits reaches a minimum and then increases as the current density is further increased. At a current density of 700 to 1 000 A·m^{-2}, the Ni content in the deposits was almost identical, regardless of temperature.

Figure 12 shows the current efficiency for Fe–Ni alloy deposition at various current densities from the solutions at different temperatures. In the solutions at all temperatures, the current efficiency for Fe–Ni alloy deposition gradually increases with the current density as a whole. The current efficiency decreases with an increase in temperature in the high-current-density region above 500 A·m^{-2}, whereas it increases with temperature at low current densities below 400 A·m^{-2}. The current efficiency in the solutions at 40°C, 50°C, and 60°C decreases once at 200, 300, and 500 A·m^{-2}, respectively. At these current densities, the Ni content in the deposits decreases toward a minimum value (Fig. 11), which suggests that the suppressive effect of $FeOH_{ad}$ on

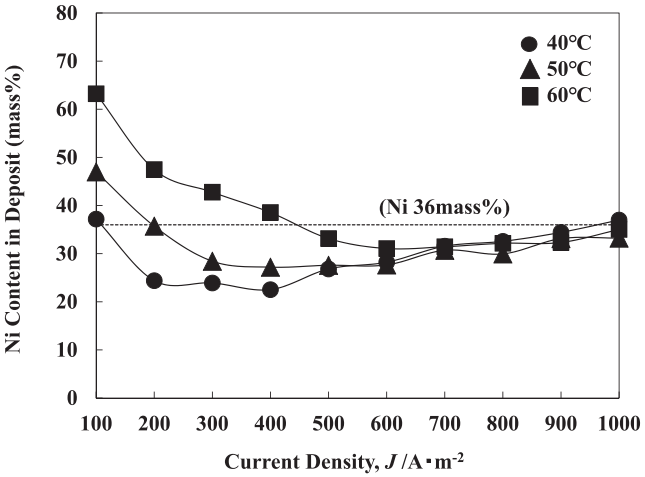

Fig. 11. Ni content in Fe–Ni alloys deposited at various current densities from solutions at different temperatures [0.394 M $FeSO_4$, pH 2.4, 250 rpm, 100–1 000 A·m^{-2}].

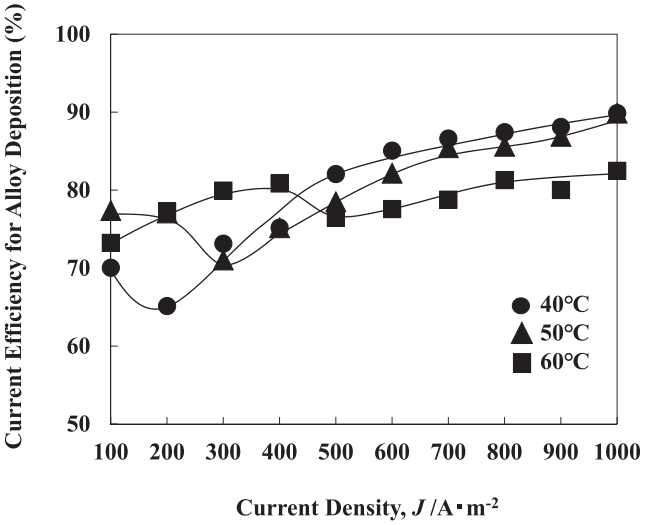

Fig. 12. Current efficiency for Fe–Ni alloy deposition at various current densities from solutions at different temperatures [0.394 M $FeSO_4$, pH 2.4, 250 rpm, 100–1 000 A·m^{-2}].

the Ni deposition reaches a maximum, thus decreasing the current efficiency.

Figure 13 shows the partial polarization curves for Fe deposition (a), Ni deposition (b), and H_2 evolution (c) from the Fe–Ni alloy solutions at different temperatures. All partial polarization curves shift toward less noble potentials with decreasing temperature. In particular, in Ni deposition, the degree of polarization increases with decreasing temperature in the region of low partial current density below 50 A·m^{-2} [Fig. 13(b)]. In other words, the suppressive effect of $FeOH_{ad}$ on the Ni deposition in the low-current-density region increases with decreasing temperature. The partial current density for hydrogen evolution significantly decreases with decreasing temperature under the condition of a high total current density.

Figure 14 shows a schematic diagram of the changes in the polarization curves for Fe–Ni alloy deposition (a) and the current density–alloy composition and current density–current efficiency curves (b) with decreasing temperature. The relationship between the current density, alloy composition, and current efficiency shown in Fig. 14(b) depends on

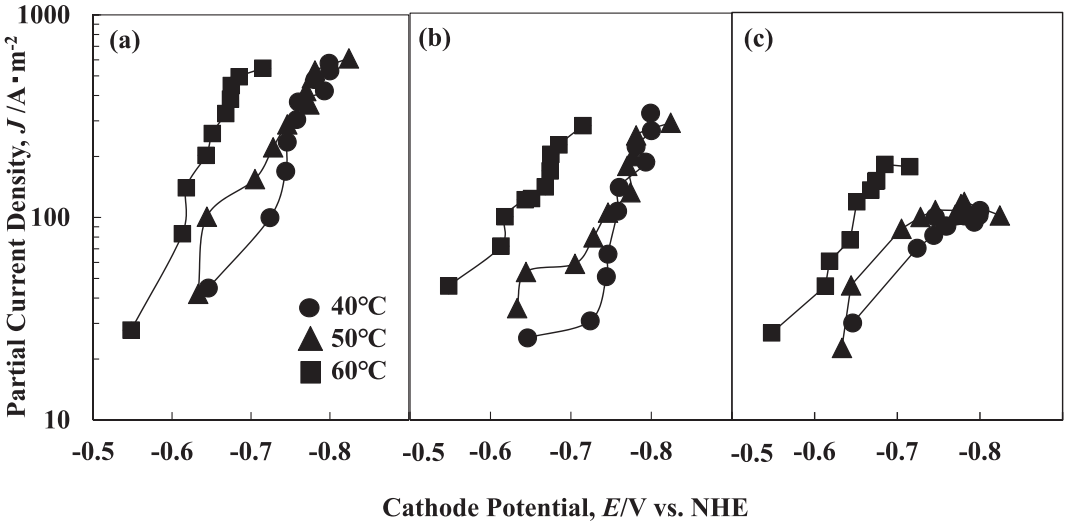

Fig. 13. Partial polarization curves for Fe (a) and Ni (b) depositions and H_2 evolution (c) from solutions at different temperatures [0.394 M $FeSO_4$, pH 2.4, 250 rpm, 100–1 000 $A \cdot m^{-2}$].

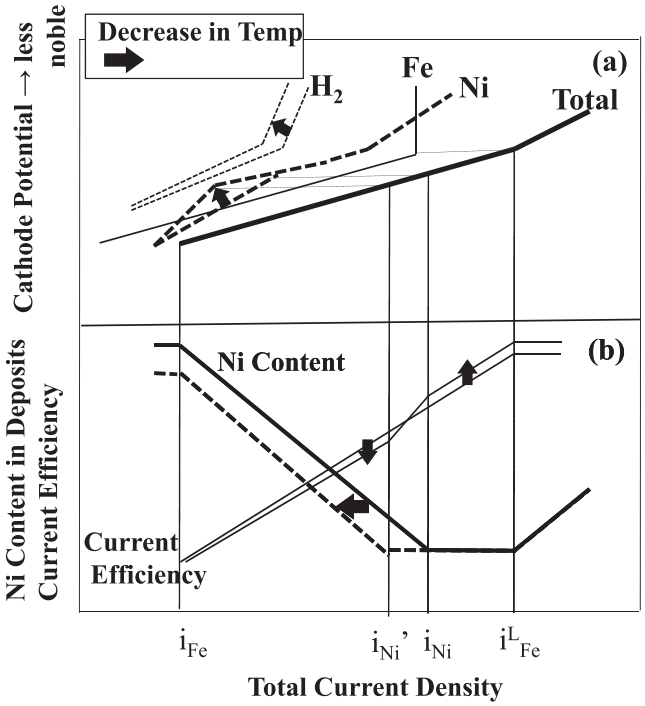

Fig. 14. Schematic diagram of the changes in the polarization curves for Fe–Ni alloy deposition (a) and current density–alloy composition and current density–current efficiency curves (b) with decreasing temperature.

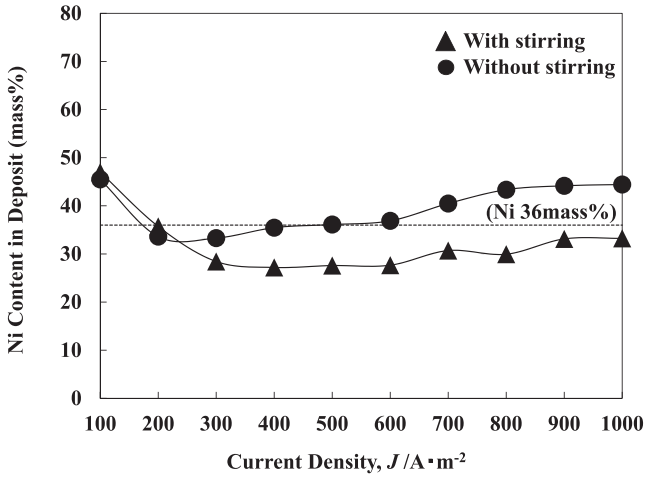

Fig. 15. Ni content in Fe–Ni alloys deposited at various current densities from solutions with and without stirring [0.394 M $FeSO_4$, pH 2.4, 50°C, 100–1 000 $A \cdot m^{-2}$].

the relative change in each partial polarization curve. When the changes in all three polarization curves with decreasing temperature (Fig. 13) are identical to each other, the effect of temperature on the current efficiency and the Ni content in the deposits is canceled. As a result, the current density–alloy composition and current density–current efficiency relationships do not change. Therefore, the relative changes in the polarization curves for Fe and Ni deposition and hydrogen evolution are important. In this study, a relatively large change in the polarization curves for Fe and Ni deposition and hydrogen evolution is reflected in the schematic diagram. As shown in Fig. 13, all the Fe and Ni depositions and hydrogen evolution are affected by the temperature, but with decreasing temperature, both the polarization of Ni deposition in the low-current-density region and the decrease in the partial current density for hydrogen evolution in the high-current-density region are remarkable. Thus, Fe deposition was assumed to be constant in Fig. 14. With decreasing temperature, since Ni deposition is more suppressed in the low-current-density region of i_{Fe} to i_{Ni}', the curve of the Ni content in the deposits as a function of current density shifts toward a lower current density. With decreasing temperature, the current efficiency increases in the high-current-density region because of the decrease in the partial current density for hydrogen evolution, and it decreases in the low-current-density region because the suppressive effect on the Ni deposition prevails.

3.4. Effect of Stirring the Solution on the Composition and Current Efficiency of the Deposited Alloy

Figure 15 shows the Ni content in the Fe–Ni alloys deposited at various current densities from stirred and unstirred solutions. The Ni content in the deposits decreases with an increase in the current density in the low-current-density region, regardless of the stirring. In a solution with stirring, the Ni content in the deposits reaches a minimum at

300 to 600 A·m^{-2} and increases at current densities above 600 A·m^{-2}. Meanwhile, in the solution without stirring, the Ni content in the deposits reaches a minimum at 200 A·m^{-2} and increases with the current density above 200 A·m^{-2}. In the stirred solution, region II shown in Fig. 3, in which the Ni content in the deposits becomes constant, becomes wider, and the current density i^L_{Fe} at which the Ni content in the deposits begins to increase is increased.

Figure 16 shows the current efficiency for Fe–Ni alloy deposition at various current densities from the solutions with and without stirring. Both with and without stirring, the current efficiency for Fe–Ni alloy deposition generally increases with current densitiy. However, the current efficiency from a solution with stirring is lower than that from a solution without stirring.

Figure 17 shows the partial polarization curves for Fe deposition (a), Ni deposition (b), and H_2 evolution (c) from the Fe–Ni alloy solutions with and without stirring. The partial polarization curves for Fe deposition (a) with and without stirring rarely change, but the potentials at which Fe deposition reaches the diffusion-limiting current of Fe^{2+} ions are −0.78 and −0.75 V with and without stirring, respectively, indicating that reaching the diffusion limitation of Fe^{2+} ions is difficult with stirring. In the partial polarization curve for Ni deposition (b), the current density increases rapidly at approximately −0.73 V without stirring, whereas it increases rapidly at approximately −0.77 V with stirring. As a result, the polarization for Ni deposition at partial current densities above 100 A·m^{-2} is higher with stirring than without stirring. These rapid increases in the Ni deposition rate at approximately −0.73 V without stirring and −0.77 V with stirring are attributed to the fact that the adsorption sites for $NiOH_{ad}$ deprived by $FeOH_{ad}$ are released as the system approaches the diffusion limitation of Fe^{2+} ions during Fe deposition, as mentioned above. With stirring, however, reaching the diffusion limitation of Fe^{2+} ions is more difficult; thus, the adsorption sites for $NiOH_{ad}$ are released less easily, resulting in an increase in the polarization for Ni deposition. On the other hand, the partial polarization curve for hydrogen evolution (c) shifts toward a noble potential with stirring in the partial-current-density region below 100 A·m^{-2}, which seems to be caused by the accelerated diffusion of H^+ ions with stirring.

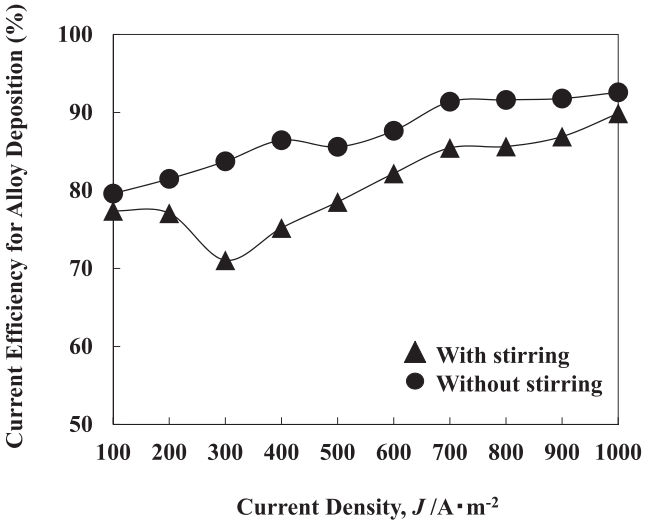

Fig. 16. Current efficiency for Fe–Ni alloy deposition at various current densities from solutions with and without stirring [0.394 M $FeSO_4$, pH 2.4, 50°C, 100–1 000 A·m^{-2}].

Figure 18 shows a schematic diagram of the changes in the polarization curves for Fe–Ni alloy deposition (a) and current density–alloy composition and current density–current efficiency curves (b) with stirring. The total current density i^L_{Fe} at which Fe deposition reaches the diffusion limitation of Fe^{2+} ions increases to i^L_{Fe}' when the solution is stirred. Therefore, the curve of the Ni content in the deposits as a function of current density in the high-current-density region shifts toward a higher current density with stirring. That is, the current density at which the Ni content in the deposits begins to increase in the high-current-density region is increased by stirring. As a result, region II, in which the Ni content in the deposits becomes almost constant, becomes wider with stirring. On the other hand, the current efficiency for Fe–Ni alloy deposition decreases with stirring in all current density regions because the partial polarization curve for hydrogen evolution shifts toward a noble potential. The polarization for Ni deposition by FeO-

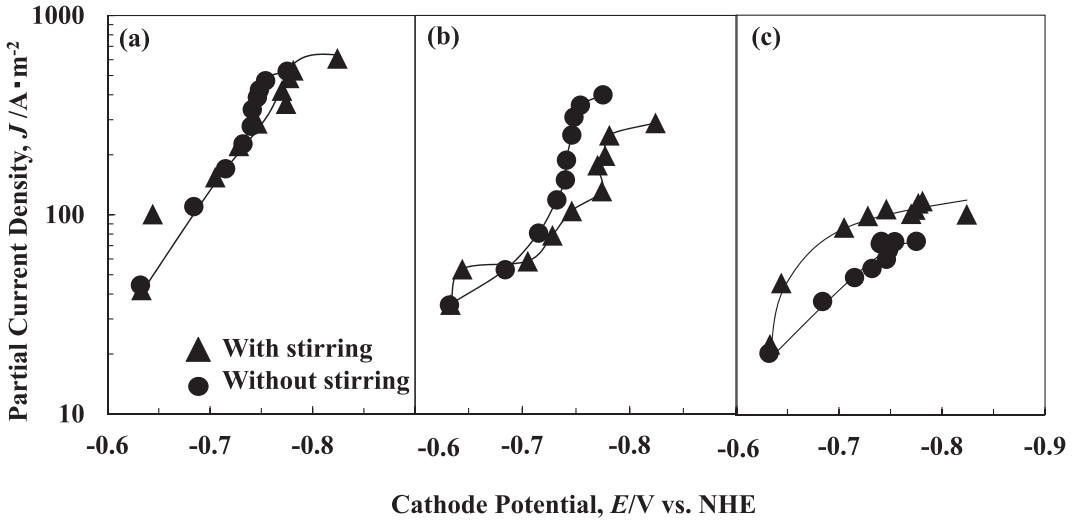

Fig. 17. Partial polarization curves for Fe (a) and Ni (b) depositions and H_2 evolution (c) from solutions with and without stirring [0.394 M $FeSO_4$, pH 2.4, 50°C, 100–1 000 A·m^{-2}].

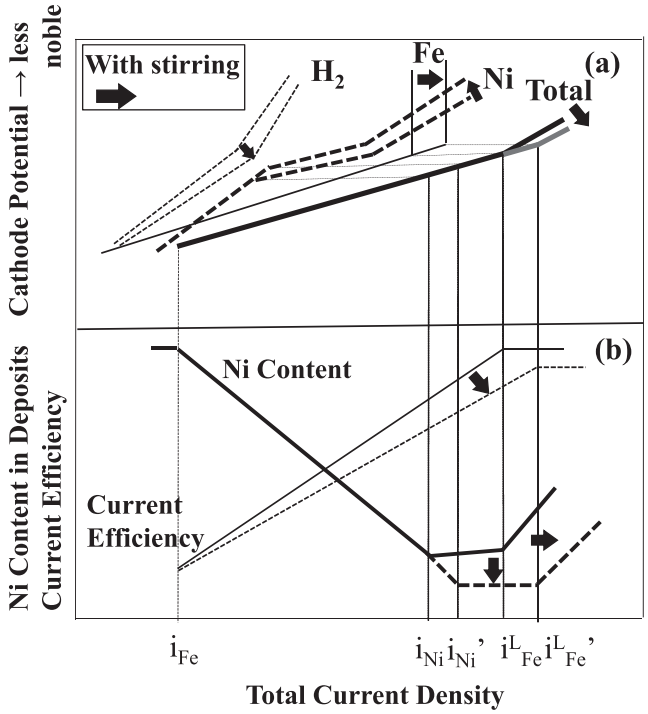

Fig. 18. Schematic diagram of the changes in the polarization curves for Fe–Ni alloy deposition (a) and current density–alloy composition and current density–current efficiency curves (b) with stirring.

H_{ad} is higher with stirring [Fig. 17(b)], which is one of the causes of the decrease in the current efficiency.

In this study, the malonic acid is added in the electrolysis solution. Although the malonic acid seems to affect the deposition behavior of Fe–Ni alloy due to its pH buffer action and the formation of complexes with Fe^{2+} and Ni^{2+} ions, the detail is unknown, and further investigation is required.

4. Conclusion

The effects of the composition, pH, temperature, and stirring of the solution on the composition of deposited Fe–Ni alloy were investigated in order to achieve the optimal Ni content of 36 mass% to minimize the thermal expansion coefficient. The Ni content in the deposits significantly decreased with increasing current density in the low-current-density region, reached a minimum, and then increased because of reaching the diffusion-limiting current density for Fe deposition as the current density increased further. With the increasing $FeSO_4$ concentration of the solution, the Ni content in the deposits decreased in the lower-current-density region, reached a constant at a low current density, and then began to increase at higher current densities. As a result, the current density region in which the Ni content in the deposits reached a minimum and then remained constant became wider with the increasing $FeSO_4$ concentration. With the decreasing pH of the solution, since the partial polarization curve for hydrogen evolution and the total polarization curve shifted toward a higher current density, the entire curve of the Ni content in the deposits as a function of current density shifted to a higher current density. With the decreasing temperature of the solution, since Ni deposition was more suppressed with the coexistence of Fe^{2+} ions, the Ni content in the deposits decreased in the low-current-density region. When the solution was stirred, the Ni content in the deposits reached a minimum as the current density increased and then began to increase at a higher current density than that without stirring because of the increase in the diffusion-limiting current density for Fe deposition. The change in the composition of the deposits owing to the electrolysis conditions can be explained by the changes in the total polarization curve and the partial polarization curves for Fe and Ni deposition and hydrogen evolution in Fe–Ni alloy deposition.

REFERENCES

1) T. Nagayama, T. Yamamoto and T. Nakamura: *J. Surf. Finish. Soc. Jpn.*, **67** (2016), 140 (in Japanese).
2) H. Saito: Physics and Application of Invar Alloys, Maruzen, Tokyo, (1978), 18 (in Japanese).
3) H. Saito and H. Fujimori: *Bull. Jpn. Inst. Met.*, **7** (1968), 263 (in Japanese).
4) H. Ise: Denchu Gizyutsu to Ouyo, Maki Shoten, Tokyo, (1996), 7 (in Japanese).
5) H. Dahms and I. M. Croll: *J. Electrochem. Soc.*, **112** (1965), 771.
6) S. Hessami and C. W. Tobias: *J. Electrochem. Soc.*, **136** (1989), 3611.
7) J. Horkans: *J. Electrochem. Soc.*, **128** (1981), 45.
8) M. Yasuda and N. Koura: *J. Met. Finish. Soc. Jpn.*, **33** (1982), 427 (in Japanese).
9) E. B. Lehman and A. Riesenkampf: *Surf. Technol.*, **11** (1980), 349.
10) W. C. Grande and J. B. Talbot: *J. Electrochem. Soc.*, **140** (1993), 669.
11) K. Y. Sasaki and J. B. Talbot: *J. Electrochem. Soc.*, **142** (1995), 775.
12) M. Matlosz: *J. Electrochem. Soc.*, **140** (1993), 2272.
13) B. C. Baker and A. C. West: *J. Electrochem. Soc.*, **144** (1997), 164.
14) J. Vaes, J. Fransaer and J. P. Celis: *J. Electrochem. Soc.*, **147** (2000), 3718.
15) H. Nakano, M. Matsuno, S. Oue, M. Yano, S. Kobayashi and H. Fukushima: *Mater. Trans.*, **45** (2004), 3130.
16) H. Nakano, M. Matsuno, S. Oue, M. Yano, S. Kobayashi and H. Fukushima: *J. Jpn. Inst. Met.*, **69** (2005), 548 (in Japanese).
17) S. Kawano, T. Ohgai, S. Kobayashi, H. Nakano, T. Tsuru, T. Akiyama, H. Fukushima and K. Hara: Proc. 2nd Int. Conf. on Processing Materials for Properties, TMS, Warrendale, PA, (2000), 769.
18) Y. Kashiwa, N. Nagano, T. Takasu, S. Kobayashi, K. Fukuda and H. Nakano: *Tetsu-to-Hagané*, **104** (2018), 593 (in Japanese).
19) T. Nagayama, Y. Mizutani, T. Nakamura and N. Shinohara: *J. Surf. Finish. Soc. Jpn.*, **57** (2006), 733 (in Japanese).
20) T. Nagayama, Y. Mizutani, Y. Kato, Y. Kotera, T. Nakamura and N. Shinohara: *J. Surf. Finish. Soc. Jpn.*, **58** (2007), 675 (in Japanese).
21) T. Yamamoto, T. Nagayama, T. Nakamura and Y. Mizutani: *J. Surf. Finish. Soc. Jpn.*, **62** (2011), 702 (in Japanese).
22) T. Nagayama, T. Yamamoto, T. Nakamura and Y. Mizutani: *ECS Trans.*, **50** (2013), No. 52, 117.
23) H. Fukushima, T. Akiyama, M. Yano, T. Ishikawa and R. Kammel: *ISIJ Int.*, **33** (1993), 1009.
24) J. O'M. Bockris and H. Kita: *J. Electrochem. Soc.*, **108** (1961), 676.
25) H. Nakano, S. Kobayashi, T. Akiyama, T. Tsuru and H. Fukushima: *Tetsu-to-Hagané*, **89** (2003), 64 (in Japanese).
26) M. Yano, H. Fukushima, H. Nakano and T. Akiyama: *Tetsu-to-Hagané*, **86** (2000), 176 (in Japanese).
27) H. Nakano, S. Arakawa, S. Oue and S. Kobayashi: *ISIJ Int.*, **53** (2013), 1864.
28) H. Nakano, S. Shibata, S. Arakawa, S. Oue and S. Kobayashi: *ISIJ Int.*, **53** (2013), 1858.
29) H. Nakano, T. Ohgai, H. Fukushima, T. Akiyama and R. Kammel: *Metall*, **55** (2001), 676.